Atomistic origins of the limited phase stability of Cs^+-rich $FA_xCs_{(1-x)}PbI_3$ mixtures

Ariadni Boziki,[†] Dominik J. Kubicki,[‡,§] Aditya Mishra,[‡] Simone Meloni,[†,‖] Lyndon Emsley,[‡] Michael Grätzel,[¶] and Ursula Rothlisberger[*,†]

†*Laboratory of Computational Chemistry and Biochemistry, Institute of Chemical Sciences and Engineering, École Polytechnique Fédérale de Lausanne, CH-1015 Lausanne, Switzerland.*

‡*Laboratory of Magnetic Resonance, Institute of Chemical Sciences and Engineering, École Polytechnique Fédérale de Lausanne, CH-1015 Lausanne, Switzerland.*

¶*Laboratory of Photonics and Interfaces, Institute of Chemical Sciences and Engineering, École Polytechnique Fédérale de Lausanne, CH-1015 Lausanne, Switzerland.*

§*Current address: Cavendish Laboratory, JJ Thomson Avenue, Cambridge CB3 0HE, United Kingdom.*

‖*Current address: Dipartimento di Scienze Chimiche e Farmaceutiche (DipSCF), Universita' degli Studi di Ferrara - Unife, Via Luigi Borsari 46, I-44121, Ferrara, Italy.*

E-mail: ursula.roethlisberger@epfl.ch

Phone: +41 (0)21 693 03 21. Fax: +41 (0)21 693 03 20

Abstract

Mixed cation perovskites, $[HC(NH_2)_2]_xCs_{(1-x)}PbI_3$, ($FA_xCs_{(1-x)}PbI_3$) with $x = 0.8$ achieve high solar cell power conversion efficiencies (PCEs) while exhibiting long-term stability under ambient conditions. In this work, we perform density functional theory (DFT) calculations, first-principles molecular dynamics (MD) simulations, solid-state

nuclear magnetic resonance (NMR) and X-ray powder diffraction (XRD) measurements aimed at investigating the possible phase stability of Cs^+-rich $FA_xCs_{(1-x)}PbI_3$, ($0 \leq x \leq 0.5$) mixed-cation materials as potential candidates for tandem solar cell applications. Estimations of the free energy of the mixtures with respect to the pure compounds together with calculations of the relative phase stability at 0 K and at finite temperature show that although the mixtures can form, the δ phase remains the thermodynamically most stable phase at room temperature. This is fully corroborated by solid-state NMR and XRD measurements and is in contrast to FA^+-rich Cs/FA mixtures where small additions of Cs^+ are sufficient to stabilize the perovskite phase at ambient conditions. The atomistic origin for this contrasting behavior arises from an energetic destabilization of the perovskite phase on the one hand caused by the incorporation of a large cation (FA^+) into the relatively small host lattice of γ-$CsPbI_3$ and on the other hand is induced by the lower degree of distortion of the host lattice. These observations allow us to propose a new design principle for the preferential stabilization of the perovskite phase over the competing δ phase.

Keywords

Halide perovskites, Mixed Cations, DFT calculations, MD simulations, Design Principle

Introduction

Over the last years, organic-inorganic hybrid lead halide perovskites have attracted great attention due to their impressive photovoltaic performance.[1–7] However, the long-term stability of perovskite solar cells remains a major challenge in order to approach commercialization. Indeed, the most widely studied material of this type, $CH_3NH_3PbI_3$ ($MAPbI_3$) has a band gap of 1.5 eV,[8] which is close to the single-junction optimum of 1.34 eV, based on Shockley's and Queisser's detailed balance considerations, with a theoretical efficiency limit of 33.16%.[9,10] In fact $MAPbI_3$ cells fabricated by regulated nucleation and Ostwald recrys-

tallization, reach an impressive PCE of 20.3%.[11] Unfortunately, $MAPbI_3$ films decompose rapidly at 423 K due to the high volatility of MAI which is prone to be attacked by polar solvents, in particular water.[7] In a similar vein, the perovskite phase of formamidinium lead triiodide $HC(NH_2)_2PbI_3$, ($FAPbI_3$) has a band gap that different experimental measurements showed to lie within the range of 1.43-1.48 eV,[7,12,13] even closer to the single-junction optimum, but the thermodynamically most stable phase at room temperature is the non-perovskite hexagonal δ-phase (yellow phase) and the transition to the perovskite phase only occurs at high temperatures ($T = 433$ K).[14]

Purely inorganic cesium lead trihalide perovskites could present an alternative since, for instance, $CsPbBr_3$ forms a perovskite structure at room temperature.[15] However, $CsPbBr_3$ has a rather wide bandgap that different experimental measurements determined to be in the range of 2.25 - 2.36 eV.[15,16] The perovskite phase of $CsPbI_3$, on the other hand has an experimental band gap of 1.73 eV,[17,18] which is close to the optimum top cell band gap for tandem solar cells of 1.7 - 1.8 eV,[19] which offers a promising way for increasing the efficiency with a minimal cost increase.[20–23] Unfortunately, $CsPbI_3$ also crystallizes in a non-perovskite hexagonal, insulating phase, the yellow δ phase at room temperature.[24] While the δ phase of $FAPbI_3$ consists of face-sharing octahedra that are surrounded by the monovalent cations, the δ phase of $CsPbI_3$ consists of edge-sharing octahedra. $CsPbI_3$ undergoes a first order phase transition from the non-perovskite to a black perovskite phase only at 600 K.[16]

This black perovskite phase has been assumed to be cubic,[16] however recently, Wang *et. al.*[25] obtained β-$CsPbI_3$ films with an extended spectral response and enhanced stability. In addition, the synchroton powder diffraction measurements of Stoumpos *et al.*[26] showed that on cooling down from temperatures above 633 K, the perovskite phase can be kinetically stable with the occurrence of tetragonal and orthorhombic structures at 533 K and 448 K, respectively. In addition, Lai *et al.*[27] also reported an orthorhombic perovskite phase for $CsPbI_3$ nanowires based on X-ray diffraction pattern measured at 300 K. Using X-ray diffraction and performing DFT calculations, Sutton *et al.*[28] demonstrated that at

room temperature, an orthorhombic structure is the most stable among the black perovskite polymorphs of $CsPbI_3$, which however remains less stable than the yellow non-perovskite form. Table 1 summarizes the different $CsPbI_3$ and $FAPbI_3$ phases.

It has also been reported that $CsPbI_3$ can adopt a black phase at room temperature by adding HI during the preparation process without any noticeable change of the optical properties of the material.[18] Despite this apparent success, the mechanism of stabilization of the black phase of $CsPbI_3$ by HI, remained unclear. It was only recently that Ke *et al.*[29] showed that the black phase does not correspond to pure $CsPbI_3$ but that a new compound, $(CH_3)_2NH_2PbI_3$ ($DMAPbI_3$) is formed, where dimethylammonium (DMA) is the HI catalyzed decomposition product of the acidic hydrolysis of the solvent dimethylformamide (DMF). In the same study, the stabilization of the black perovskite phase of $CsPbI_3$ through mixing with DMA was demonstrated. In particular, the mixed cation compound $Cs_{0.7}DMA_{0.3}PbI_3$ achieved a maximum PCE of 12.62% and has a band gap of around 1.7 eV.

Table 1: Different phases of $CsPbI_3$ and $FAPbI_3$[24,28,30]

Crystal structure	Crystal system	Space group	Thermodynamic stability	Temperature range
δ-$CsPbI_3$	orthorhombic	*Pnma*	stable	$\leq$ 600 K
γ-$CsPbI_3$	orthorhombic	*Pnam*	metastable	$\leq$ 448 K
β-$CsPbI_3$	tetragonal	*P4-mbm*	metastable	448 K - 533 K
cubic-$CsPbI_3$	cubic	*Pm-3m*	stable	$\geq$ 600 K
δ-$FAPbI_3$	hexagonal	$P6_3mc$	stable	$\leq$ 433 K
β-$FAPbI_3$	trigonal	*P3*	metastable	$\geq$ 150 K
α-$FAPbI_3$	trigonal	*P3m1*	stable	$\geq$ 433 K

Summarizing, although the most studied single-cation compounds possess band gaps either close to the optimum for single-junction or top cell in tandem solar cells, they are thermodynamically not stable in the perovskite phase over a sufficient temperature range. To overcome this problem, a design protocol has been introduced that mixes different monovalent cations and halides achieving an enhanced thermal and structural stability.[31–33]

Indeed, Pellet *et al.*[31] produced cells with an enhanced short-circuit current by using a

mixture of FA^+ and MA^+ as monovalent cations. However, similar to $MAPbI_3$ films, the mixed compounds are also prone to decomposition at high temperatures. To circumvent problems related to thermal decomposition of MA^+, cesium has attracted attention for use in mixed organic-inorganic lead halide perovskites. Choi *et al.*[34] presented cesium-doped $MAPbI_3$ cells, achieving an efficiency of 7.68% upon addition of 10% cesium. Moreover, Lee *et al.*[35] presented mixtures of cesium and formamidinium with enhanced thermal and humidity stability, achieving a power conversion efficiency of 16.5%. We have shown previously that the addition of Cs^+ into $FAPbI_3$ leads to a reduction of the phase transition temperature by $\sim$ 200 - 300 K, explaining why the perovskite phase becomes stable at room temperature for $Cs_xFA_{(1-x)}PbI_3$ compounds.[36] Furthermore, Saliba *et al.* proposed a triple cation perovskite compound, which consists of Cs^+, FA^+ and MA^+, achieving a PCE of 18 %.[32] Hence, it appears that Cs^+ is highly efficient in suppressing the black-to-yellow phase transition in 3D perovskites based on FA^+ as the majority cation. Li *et al.*[37] suggested that tuning the Goldschmidt tolerance factor[38,39] and its extension to organic cations proposed by Kieslich *et al.*,[40,41] through solid-state alloying could be a way to stabilize the black perovskite structure. Specifically, the authors report that by mixing $FAPbI_3$ with $CsPbI_3$, the effective tolerance factor can be tuned and mixtures of low Cs^+ concentration, which are stable in the perovskite phase, can be formed.

In contrast to the FA^+-rich case of FA/Cs mixtures, Cs^+-rich compounds have been less investigated so far although they might be promising candidates for tandem solar cells.[20–23] In this work, we set out to investigate the stability of Cs^+-rich, $FA_xCs_{(1-x)}PbI_3$ mixtures, for FA^+ concentrations up to 50%, through a combination of DFT calculations, MD simulations and experiments. The goal of our investigation is to examine if stable Cs^+-rich mixtures can be formed and if they lead to the desired stabilization of the perovskite phase. We first evaluate the free energy for the mixtures with respect to the pure phases, in order to establish if mixing is possible and if it leads to any preferential stabilization of the perovskite phase with respect to the δ phase. In addition, the energy difference between the δ and the

perovskite phase at 0 K provides a first indication about the relative stability of the two phases and MD simulations are used to gain information about the relative phase stability at finite temperature. Taken the results of our studies together, we show that although stable mixtures can be formed they do not lead to significant extensions of the stability range of the perovskite phase. This is also corroborated by solid-state NMR and XRD measurements which show the formation of stable mixed Cs/FA δ phases at room temperature. Evaluation of the structural characteristics of the mixed compounds reveals possible reasons for this contrasting behavior between FA^+-rich versus Cs^+-rich FA/Cs perovskites. Calculations of the optical properties of the metastable Cs^+-rich perovskite materials show that they would be potential candidates for solar cells applications, motivating a search for alternative ways of preparation.

Results and discussion

Properties of $CsPbI_3$

As mentioned above, it is now well-known that apart from the two thermodynamically stable phases of $CsPbI_3$; a non-perovskite δ-phase from 0 up to 600 K and a cubic perovskite phase above 600 K (Figure 1),[16] two more kinetically stabilized black perovskite phases with distorted octahedra have been observed. These phases are known as β and γ phases, respectively, with the orthorhombic γ-$CsPbI_3$ (Figure 2) being the most stable one among the perovskite polymorphs at room temperature, but still remaining less stable than the yellow non-perovskite phase.[26,28] For this reason, in our study we have taken the three phases, δ, γ as well as the high temperature cubic phase into account.

The calculated single-particle Kohn-Sham band gap of the cubic perovskite phase within the fully **k**-point converged unit cell at 0 K, as predicted by calculations employing the PBE functional,[42] is 1.44 eV, in good agreement with other theoretical studies,[43,44] but somewhat in contrast to the experimentally measured band gap of 1.73 eV.[17,18] To make a meaningful

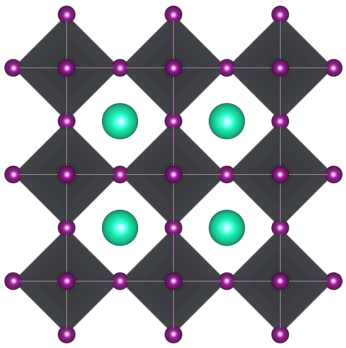

Figure 1: DFT optimized structure of cubic-$CsPbI_3$.

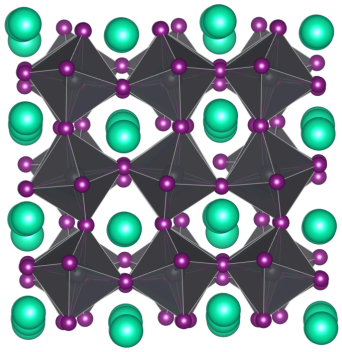

Figure 2: DFT optimized structure of the γ-$CsPbI_3$.

comparison with the experimental data, which has been measured at finite temperature, thermal effects should also be taken into account. The thermal effects can fully be taken into account by performing first-principles MD simulations at finite temperature. For this reason, we performed Car-Parrinello MD simulations of 5.4 ps in the *NVT* ensemble at a temperature of 300 K, for a cubic $CsPbI_3$ supercell of 320 atoms at the gamma point. The 0 K band gap of this real-space equivalent of the fully **k**-point converged sample is 1.39 eV. Figure 3 shows the histogram of the band gaps for different finite temperature configurations, allowing to calculate the contribution of temperature effects on the 0 K band gap. We find that this contribution is as large as 0.49 eV. This is unusually large, since in previous studies, contributions of thermal effects to the band gap, for similar types of materials, are of the order of 0.15 eV.[45] However, it is worth mentioning that Wiktor *et al.*[43] also estimated a 0.47 eV contribution of thermal effects to the 0 K gap of cubic $CsPbI_3$, employing the

rVV10 functional.[46,47] Summarizing, the calculated finite temperature band gap is 1.83 eV comparable with the experimental band gap.[17,18]

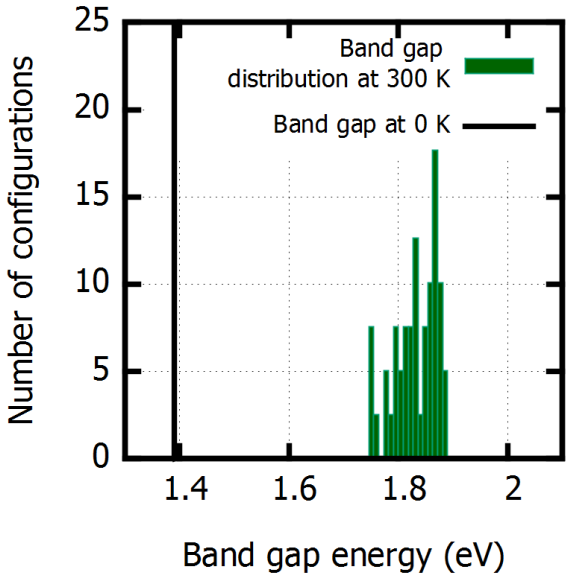

Figure 3: Histogram of the thermal distribution of the band gap compared to the value at 0 K for the cubic phase of $CsPbI_3$.

Since the metastable γ-$CsPbI_3$ phase is the most stable among the different perovskite polymorphs at room temperature, we also examined the orthorhombic structure with a cell containing 240 atoms. The fully DFT optimized structure at 0 K has average Pb-I-Pb angles of 155° versus 154° of the experimental orthorhombic $CsPbI_3$.[28] The fully converged, **k**-point sampled 0 K band gap is 1.77 eV. As shown in Figure S1 of Supporting Information, thermal effects at 300 K are much smaller than in the case of cubic-$CsPbI_3$ and amount to 0.1 eV only. The significant difference between the thermal effects of the cubic and the orthorhombic cell can be explained by considering the nature of the valence band maximum (VBM) which is formed by an antibonding combination of I p and Pb s orbitals.[44] In cubic-$CsPbI_3$, on the one hand, the distortions induced by the dynamic disorder of the lattice at finite temperature lead to a reduction of the antibonding overlap and in turn to an increase of the band gap. In γ-$CsPbI_3$, on the other hand, since the lattice is already orthorhombic the dynamic disorder at finite temperature induces only further distortions that lead to only a

slight reduction of the antibonding overlap and a slight increase of the band gap, respectively. For completeness, we considered both the orthorhombic as well as the cubic phases in the subsequent investigation of the mixed-cation phases of $FA_xCs_{(1-x)}PbI_3$.

Mixed $FA_xCs_{(1-x)}PbI_3$ compounds ($0 \leq x \leq 0.5$)

In order to study if mixed-cation compounds in the three phases δ, γ and cubic are stable and if any preferential phase stabilization takes place upon mixing, we performed structural relaxations (atomic positions and cell parameters) of the mixed $FA_xCs_{(1-x)}PbI_3$ compounds at 0 K and computed the mixing internal energy and entropy. We remark that for computing the mixing internal energy of the perovskite phases we used β-$FAPbI_3$ as a reference.[24]

$$\begin{aligned} \Delta E_{phase}(FA_xCs_{(1-x)}PbI_3) = E_{phase}(FA_xCs_{(1-x)}PbI_3) \\ - [xE_{phase}(FAPbI_3) \\ + (1-x)E_{phase}(CsPbI_3)] \end{aligned} \tag{1}$$

$$T\Delta S_{phase}(FA_xCs_{(1-x)}PbI_3) = -k_BT[xlnx + (1-x)ln(1-x)] \tag{2}$$

Analysis of the energetic contribution to the mixing free energy, which is expressed by equation (1) shows that in the case of the δ phase, replacement of Cs^+ by FA^+ leads to destabilization (energy increase) with respect to the pure FA and/or $CsPbI_3$ δ phases (magenta line in Figure 4 upper panel). The mixing entropy contribution to the free energy expressed by equation (2) and calculated at room temperature, (298 K), only partially compensates this penalty. Similarly, in the γ phase, mixing induces almost no or slightly positive energetic contributions (Figure 4, bottom panel, magenta line) and the estimated free energy of mixing is close to zero (Figure 4, bottom panel, black line). Indeed, for both cases, δ and γ phases, (excluding only the δ-$FA_{0.33}Cs_{0.67}PbI_3$, where mixing leads to destabilization with respect to the pure phases) the estimated free energy of mixing is of the order of 0.006 eV

per stoichiometric unit, which is smaller than the typical variations among different substitution patterns. Since these values lie within the intrinsic error of the calculations, we cannot conclude if mixing in orthorhombic γ and δ phases leads to marginally stable, or slightly unstable compounds with respect to the pure phases.

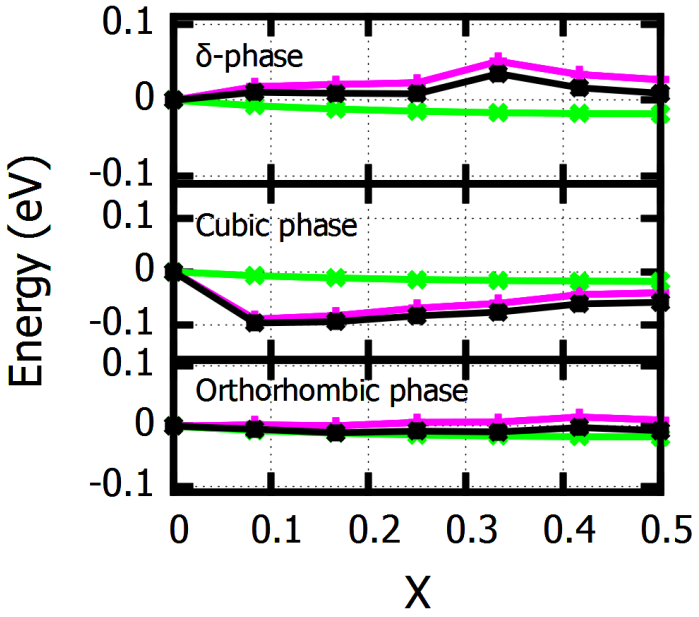

Figure 4: Variation of the free energy, of $FA_xCs_{(1-x)}PbI_3$ expressed as $\Delta F = \Delta E$ - $T\Delta S$ (black line), the internal energy, ΔE (magenta line), and the mixing entropy contribution, -$T\Delta S$ (with T=298 K, light-green line), as a function of FA^+ ratio. In the top graph the variations of free energy, enthalpy and mixing entropy contribution are estimated with respect to the pure δ phases. In the middle and bottom graphs each contribution to the free energy is estimated with respect to cubic-$CsPbI_3$ and γ-$CsPbI_3$, respectively.

In contrast, cation mixing is already favored by the energetic contribution when cubic-$CsPbI_3$ is employed as reference, (Figure 4 central panel). As expected, the mixing entropy contribution further favors the stabilization of the perovskite phase, leading to a stability maximum around $FA_{0.08}Cs_{0.92}PbI_3$ with respect to the pure compounds. One should mention here that the calculation of any possible stabilization of the mixtures with respect to the cubic-$CsPbI_3$ does not imply that the mixtures adopt the cubic phase as well. In fact, cation mixing induces a sizable distortion on the cubic phase resulting in optimized structures of orthorhombic type for the mixtures, *i.e.* with all the three tilting angles different from zero.

An issue that demands further investigation is if the inclusion of zero point energy and vibrational entropy contributions influence the relative free energies. Calculations of the vibrational entropy term are not trivial in the case of perovskites. Indeed, both harmonic and quasi-harmonic phonon calculations lead to imaginary modes, which have no physical meaning.[48] In our case, since we are considering relative stabilities within the same crystallographic phase, we consider these relative differences to a first approximation to be small but still able to influence the stability trend of the mixing free energy with respect to the pure phases.

We use the energy difference at 0 K as a first indicator of the relative stability of the perovskite and the δ phases. As shown in Table 2, δ-$CsPbI_3$ has a lower energy at 0 K, which is consistent with the experimental data that predict the δ phase to be the most stable low temperature phase.[24] However, when considering cation mixing in the cubic-$CsPbI_3$, FA^+ substitution leads to a reduction of the energy difference by roughly half, independent of the FA^+ doping level. On the contrary, FA^+ mixing in γ-$CsPbI_3$ reduces the energy difference with the δ phase by only 14 - 21% up to 25% of FA^+ and 21 - 36% for higher doping levels up to 50% FA^+. As previously, the mixed-cation phases are orthorhombic rather than cubic as soon as the mixtures are generated, explaining why the energy differences with the δ phase for cubic and orthorhombic are the same at all FA^+ contents. It is interesting to compare the effect of Cs^+ mixing in $FAPbI_3$ with FA^+ mixing in $CsPbI_3$. In the case of $FAPbI_3$, the most stable perovskite phase is the β one, which is more distorted with respect to the other known perovskite phase of $FAPbI_3$, the α phase. At variance with FA^+ mixing into γ-CsPbI3, Cs^+ mixing in β-$FAPbI_3$ reduces the energy difference between the δ and the β $FAPbI_3$ phase at 0 K by only 8% for a doping level of 8% Cs^+ and to 17% for doping levels up to 25% Cs^+. For higher doping levels up to 50% Cs^+, the energy difference is reduced by 33%. We also report the Goldschmidt tolerance factors of both the pure compounds and the mixtures (Table S1 of Supporting Information).

To shed more light on the finite temperature phase stability, we performed MD simula-

Table 2: Relative energetic stability, expressed by $\Delta E_{a\delta} = E_a - E_\delta$ per stoichiometric unit of the cubic/orthorhombic perovskite phase with respect to the δ phase upon doping of $CsPbI_3$ with FA^+

	Difference in energy (per stoichiometric unit) between perovskite and δ phases at 0 K (eV)	
Fraction of FA^+ doped into $CsPbI_3$ structure	Reference structure cubic-$CsPbI_3$	Reference structure γ-$CsPbI_3$
0%	0.23	0.14
8%	0.12	0.12
17%	0.11	0.11
25%	0.12	0.12
33%	0.09	0.09
42%	0.11	0.11
50%	0.11	0.11

tions at 300 K employing the *NVT* ensemble at the gamma point for δ and orthorhombic $FA_{0.33}Cs_{0.67}PbI_3$ compounds, using simulation cells of 176 atoms. From the average potential energy of an equilibrated trajectory of 2.2 ps, as shown in Figure 5, we conclude that the δ phase is still the more stable phase at room temperature. In addition, within the time scale of these simulations and taking into account that our systems are not containing any vacancies that could cause diffusion, no phase segregation towards the pure phases was observed. This behavior is expected, since as has been reported by previous studies the diffusion barriers for cations such as Cs^+ and FA^+ are very large and diffusion could only be observed on very long time scales.[49]

We have verified the theoretical predictions by synthesizing $FA_{0.08}Cs_{0.92}PbI_3$ and $FA_{0.16}Cs_{0.84}PbI_3$ using solid-state mechanosynthesis[50–52] and characterizing them using solid-state magic angle spinning (MAS) NMR (Figure 6). Our group and others have previously shown that solid-state NMR,[53–61] and in particular ^{133}Cs,[58,62–66] can be used to probe the atomic-level microstructure of halide perovskites. Cesium environments corresponding to Cs^+ incorporated into the 3D perovskite lattice of α-$FAPbI_3$ (Figure 6a, 13 ppm, FWHM (1169 ± 20) Hz), Cs^+ inside the black orthorhombic γ-$CsPbI_3$ 3D perovskite (Figure 6b, 154 ppm, FWHM (440 ± 4) Hz) and yellow non-perovskite δ-$CsPbI_3$, (Figure 6c, 242 ppm,

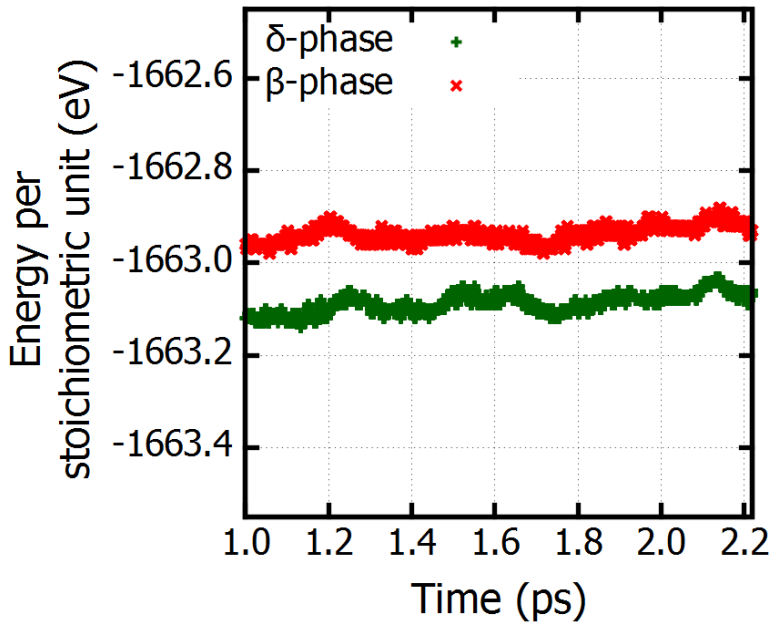

Figure 5: Potential energies per stoichiometric unit for each frame for the δ and the perovskite $FA_{0.33}Cs_{0.67}PbI_3$ mixtures across a 2.2 ps trajectory derived by MD simulations. The δ phase is always more stable than the perovskite one.

FWHM (353 ± 4) Hz) are characterized by distinct and unambiguous shifts in ^{133}Cs MAS NMR spectra. The as-prepared powders of $FA_{0.08}Cs_{0.92}PbI_3$ and $FA_{0.16}Cs_{0.84}PbI_3$ are yellow and their color is not affected by annealing at 170 °C. Their spectra (Figure 6d, e) contain a peak which is identical to that of δ-$CsPbI_3$, confirming the non-perovskite nature of these Cs^+-rich $FA_xCs_{(1-x)}PbI_3$ phases.

That said, in both spectra there is an overlapping broad component ($FA_{0.16}Cs_{0.84}PbI_3$: fitted shift of 236 ppm and FWHM (1885 ± 30) Hz) which corresponds to a distribution of structurally disordered cesium environments due to the incorporation of FA^+ into the non-perovskite δ-$CsPbI_3$ structure. We corroborate this hypothesis by measuring ^{1}H and ^{13}C CP MAS NMR spectra of the mixed-cation $FA_{0.16}Cs_{0.84}PbI_3$ material (Figure 6h, 6k) and comparing them to those of α-$FAPbI_3$ (Figure 6f, 6i) and δ-$FAPbI_3$ (Figure 6g, 6j). For both nuclei, the FA resonances of $FA_{0.16}Cs_{0.84}PbI_3$ are significantly shifted with respect to those

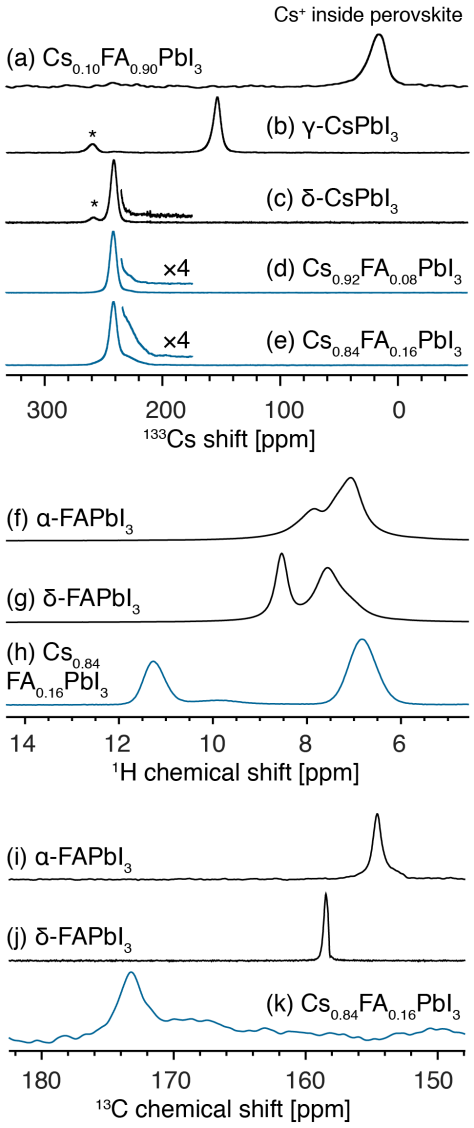

Figure 6: Solid-state MAS NMR characterization of the materials. ^{133}Cs spectra at 11.7 T, 298 K and 22 kHz MAS of (a) $FA_{0.9}Cs_{0.1}PbI_3$, (b) γ-$CsPbI_3$, (c) δ-$CsPbI_3$, (d) $FA_{0.08}Cs_{0.92}PbI_3$, (e) $FA_{0.16}Cs_{0.84}PbI_3$. ^{1}H and ^{13}C spectra at 21.1 T, 100 K and 12 kHz MAS of (f, i) α-$FAPbI_3$, (g, j) δ-$FAPbI_3$, (h, k) $FA_{0.16}Cs_{0.84}PbI_3$. The asterisks (*) indicate an impurity phase (Cs_4PbI_6).[66]

of the reference phases, confirming that FA^+ is present in a new microscopically different chemical environment and that there is no phase segregation into pure α-$FAPbI_3$ or δ-$FAPbI_3$, in contrast to previous experimental results, suggesting that for high Cs^+ concentrations, phase separation to the pure δ phases is observed.[37] We note that the ^{1}H peak at 11.3 ppm

is likely a side product of the reaction when it is carried out at this stoichiometric ratio since it has a significantly different T_1 (23 s) than that of the FA peak (6.8 ppm, T_1=14 s). If the two peaks belonged to the same phase, ^{1}H-^{1}H spin diffusion would act to equalize their relaxation times, which is not the case here. The solid-state NMR results are also consistent with the XRD patterns of the materials (Figure S3, Figure S4 of Supporting Information), whereby the mixed phases show reflections corresponding to δ-$CsPbI_3$ which are broadened due to the presence of static chemical disorder. In addition, the longitudinal relaxation time, T_1, of FA in $FA_{0.16}Cs_{0.84}PbI_3$ is significantly longer (14 s) compared to that of α-$FAPbI_3$ (2.5 s) δ-$FAPbI_3$ (1 s). T_1 relaxation in protonated solids depends on the strength of the ^{1}H-^{1}H dipolar interaction,[62] and the spectral density at ^{1}H Larmor frequency. While the dipolar interaction that drives relaxation is largely intramolecular and is not expected to change between phases, differences in spectral density reflect the different extent of residual motion present at 100 K. This allows us to further corroborate that the FA environments in $FA_{0.16}Cs_{0.84}PbI_3$ are microscopically different than those of δ-$FAPbI_3$ and α-$FAPbI_3$.

Taken together, the theoretical analysis and the experimental results confirm that in contrast to the FA^+-rich case, Cs^+-rich mixed perovskite phases are not thermodynamically stable at room temperature. We therefore study the reasons why in contrast to the FA^+-rich case, mixing in the γ phase is enthalpically significantly disfavored. An analysis of the structural characteristics of the mixed compounds allows us to rationalize the destabilization of the Cs^+-rich mixtures in the γ phase. The calculated volume per stoichiometric unit of γ-$CsPbI_3$ (252.73 Å^3) is 7.3 % smaller than that of α-$FAPbI_3$ (272.58 Å^3). Upon FA^+ doping into the γ-$CsPbI_3$ lattice, the available volume for the monovalent cation is thus decreased.

In addition, following the evolution of the volume upon FA^+ doping into $CsPbI_3$ (Figure 7), even in the case of cubic-$CsPbI_3$, we observe an abrupt decrease on going from the pure compound to the lowest concentration (8 %), consistent with a transition from cubic to orthorhombic phase, due to the lowering of symmetry and cubooctahedral distortion upon cation substitution. This is also manifested in the average Pb-I-Pb angle distribution (Figure

8), which moves from an average of 180° (characteristic of the cubic phase) to 155° at low FA^+ doping ratios, indicating the adoption of an orthorhombic phase. This can again be explained by the difference in ionic radii of Cs^+ and FA^+. In this case, the smaller Cs^+ is substituted by the larger FA^+, imposing less distortions in the lattice. On increasing the FA^+ doping level, the volume of the cell is increasing proportionally, leading at 50 % of doping to a volume which is larger than that of the initial cubic perovskite phase. The inclusion of more FA^+ alleviates the initial strain in the γ-$CsPbI_3$, which also explains the gradual increase of the Pb-I-Pb angle distribution at high FA^+ concentrations. Due to the antibonding character of the VBM,[44] the reduction of the lattice distortion leads to an increase of the overlap between the I p and Pb s orbitals (Figure 9), which in turn leads to an energy increase (destabilization) of the mixed perovskite phases.

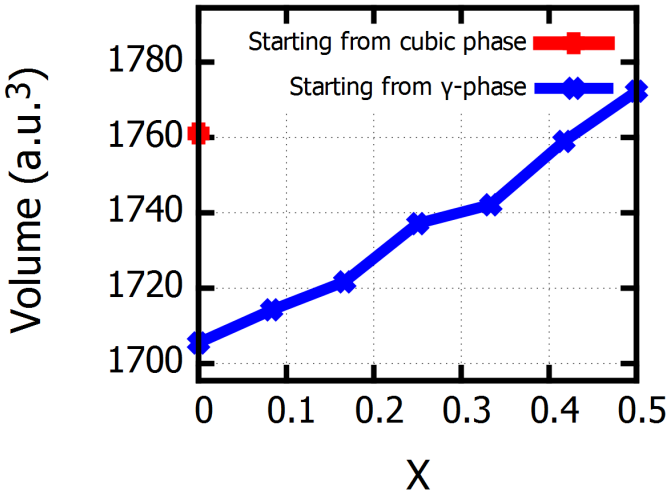

Figure 7: Volume evolution upon FA^+ doping into $CsPbI_3$. Red and blue indicate results obtained by starting from the pure cubic, respectively orthorhombic phase.

Having characterized the structural properties of the mixed-cation compounds, we now turn to an analysis of their electronic properties. Several studies have shown that PBE-GGA, without the inclusion of spin-orbit coupling effects (SOC) provides fortuitous good predictions of the band gap of lead halide perovskites.[67,68] Table 3 shows the evolution of the calculated band gaps for the metastable perovskite phases, using this protocol. It is

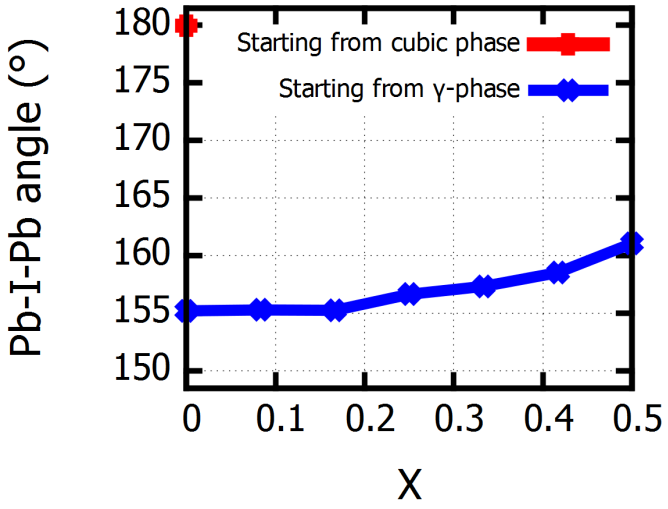

Figure 8: Average Pb-I-Pb angles evolution upon FA^+ doping into $CsPbI_3$. Red and blue indicate results obtained by starting from the pure cubic, respectively orthorhombic phase.

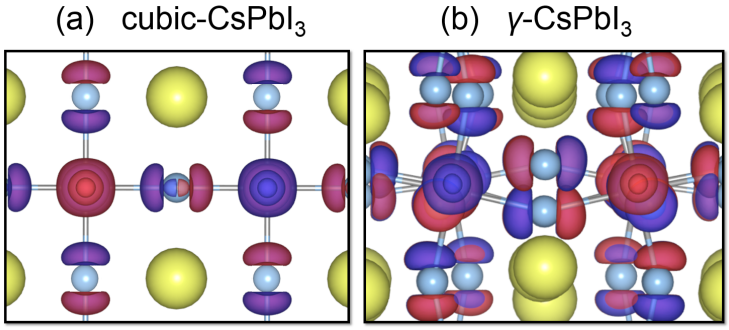

Figure 9: Antibonding overlap between the I p and Pb s orbitals of the VBM. Yellow, cyan and silver indicate Cs^+, I^- and Pb^{2+}, respectively. The orbitals are represented with blue and red. Upon moving from the cubic structure (a) to the orthorhombic (b) the lattice distortion increases, leading to a reduction of the antibonding overlap.

obvious that upon mixing, the band gap remains remarkably unaffected, with values close to the optimum for tandem solar cell applications. We observe that the highest band gap values correspond to the most distorted orthorhombic structures, consistent with the well-known electronic characteristics of the VBM of organic-inorganic lead halide perovskites, in which the overlap between I p and Pb s orbitals is reduced on going from the cubic to the orthorhombic phase.[44,69]

Table 3: Average DFT/PBE 0 K band gaps of cubic/orthorhombic $CsPbI_3$ and of Cs^+-rich $FA_xCs_{(1-x)}PbI_3$ mixtures as a function of different FA^+ concentrations. The standard deviation indicates variations due to different substitution patterns.

Fraction of FA^+ into $CsPbI_3$	Band gap (eV)
0%	1.44 (cubic-$CsPbI_3$)
0%	1.77 (γ-$CsPbI_3$)
8%	1.81
17%	1.81 ± 0.03
25%	1.80 ± 0.02
33%	1.79 ± 0.02
42%	1.79 ± 0.01
50%	1.74 ± 0.03

Conclusions

The static DFT/PBE calculations, MD simulations, solid-state NMR and XRD measurements show that in contrast to the FA^+-rich case, the perovskite phase of Cs^+-rich $FA_xCs_{(1-x)}PbI_3$ mixtures ($0 \leq x \leq 0.5$) is thermodynamically unstable at room temperature. The energy difference between the δ and γ phases at 0 K, shows that the δ phase is more stable for both the pure and the mixed compounds. Furthermore, MD simulations at room temperature predict that the mixtures are stable at least within the time scale of the simulations and that the δ phase is preferred. This observation is also supported by solid-state NMR and XRD measurements suggesting that stable mixed-cation phases are formed and adopt the δ phase.

The contrasting behavior between FA^+-rich and Cs^+-rich $FA_xCs_{(1-x)}PbI_3$ mixtures can be explained in terms of the enthalpic penalty caused through the incorporation of the relatively large FA^+ cation into the limited available space of the γ-$CsPbI_3$ orthorhombic lattice that enforces a structural transition towards a more cubic-like lattice where the space for the monovalent cation is larger. This structural change increases the antibonding overlap of the I p-orbitals with the s-orbitals of Pb of the VBM leading to a less stable structure. This behavior is contrary to the FA^+-rich case, where the incorporation of Cs^+ into α-$FAPbI_3$

leads to a distortion of the cubic host lattice towards a more orthorhombic structure, in which the antibonding overlap of the I p-orbitals with the s-orbitals of Pb of the VBM is lowered, leading to a more stable structure with larger band gap. These observations suggest a new design principle for the maximization of the preferential stabilization of the perovskite phase over the competing δ phases. According to which, there is a higher chance to favor the stabilization of the perovskite phase over the δ phase by using cubic-like phases as the host lattice. On the contrary, the incorporation of a large cation into a relatively small and already distorted 3D perovskite lattice reduces the stabilization of the perovskite phase over the δ phase. Finally, the calculation of the band gaps of the mixed compounds indicates that if the perovskite phase can be kinetically trapped, it would be a potential candidate for tandem solar cell applications.

Computational details

DFT[70,71] calculations have been performed using the Quantum Espresso suites of codes.[72,73] The Generalized Gradient Approximation (GGA) to DFT in the Perdew-Burke-Ernzerhof (PBE) formulation has been used.[42] The interactions between valence electrons and core electrons and nuclei are described by ultrasoft pseudopotentials.[74] The Kohn-Sham orbitals are expanded in a plane wave basis set with a kinetic energy cutoff of 40 Ry and a density cutoff of 240 Ry. The Brillouin zone is sampled with a 4x4x4 Monkhorst-Pack k-points shifted grid.[75] These values have been chosen after having performed convergence tests for the total energy, the band gap, the pressure, the stresses and the atomic forces. SOC effects are not explicitly included in the calculations due to the well-known fortuitous error cancellation of SOC and many-body effects in the case of lead halide perovskites.[67]

Comparing the absolute energy of Kohn-Sham orbitals in solid state systems is not trivial since for an infinitely periodic system there is no reference value for the energy origin. A technique to cope with this problem is to use localized deep impurity states or states that

are expected to be unaffected by the chemical and structural nature of the system such as semicore or core states. As a reference, an approach analogous to the one used by Alkauskas *et al.*[76] for band alignment in solids has been employed here, where the energy of the Pb_{5d} semicore state is used as reference.[44] This is the only band which is rigidly shifted, something that supports the idea that the vacuum level of these atomic orbitals is independent of the system.[44]

For the mixed compounds, the structures have been prepared starting from the experimental cubic phase of $CsPbI_3$, replacing Cs^+ by FA^+ in different ratios. All the structures consist of superlattices that contain 12 stoichiometric units. For each stoichiometry, when allowed, we considered 10 different possible replacements, starting from the energetically lowest configuration at the next lower FA^+ content. The structures were fully relaxed (atomic positions and cell parameters). The maximum standard deviation of the difference in energy per stoichoiometric unit among the different configurations is of the order of 0.006 eV.

Car-Parrinello MD simulations in the *NVT* ensemble were performed using the CPMD code.[77] The wavefunction cutoff was set to 90 Ry and Goedecker normconserving pseudopotentials were used.[78–80] A time step of 5 a.u. was used with a fictitious mass parameter of 800 a.u.. The temperature in the simulations was set to 300 K and was controlled by a Nosé-Hoover thermostat with a coupling frequency of 1000 cm^{-1}.[81–83]

Experimental details

Perovskite mechanosynthesis: Starting materials were stored inside a glove box under argon. Perovskite powders were synthesized by grinding the reactants in an electric ball mill (Retsch Ball Mill MM-200) using a grinding jar (10 ml) and a ball (ø10 mm) for 30 min at 25 Hz. The resulting powders were annealed for 5 minutes at temperatures specified below. The amounts of reagents taken into the synthesis were as follows:

- δ-$FAPbI_3$: 0.172 g formamidinium hydroiodide (1.00 mmol) and 0.461 g PbI_2 (1.00

mmol). No annealing.

- α-$FAPbI_3$: δ-$FAPbI_3$ was annealed at 170 °C to induce the phase transition
- δ-$CsPbI_3$: 0.260 g CsI (1.00 mmol) and 0.461 g PbI_2 (1.00 mmol). No annealing
- γ-$CsPbI_3$: δ-$CsPbI_3$ was annealed at 350 °C to induce the phase transition to the α phase. After cooling to room temperature the black γ phase is obtained and the material transforms back to the δ phase with a half-life of about 1 hour.
- $FA_{0.9}Cs_{0.1}PbI_3$: 0.154 g of FAI (0.90 mmol), 0.026 g of CsI (0.10 mmol) and 0.461 g of PbI_2 (1.00 mmol). The material was annealed at 120 °C.
- $FA_{0.08}Cs_{0.92}PbI_3$: 0.014 g of FAI (0.08 mmol), 0.234 g of CsI (0.90 mmol) and 0.461 g of PbI_2 (1.00 mmol). The material was annealed at 170 °C.
- $FA_{0.16}Cs_{0.84}PbI_3$: 0.028 g of FAI (0.16 mmol), 0.218 g of CsI (0.84 mmol) and 0.461 g of PbI_2 (1.00 mmol). The material was annealed at 170 °C.

Solid-state NMR measurements: Room temperature ^{133}Cs (65.6 MHz) NMR spectra were recorded on a Bruker Avance III 11.7 T spectrometer equipped with a 3.2 mm CPMAS probe. Low-temperature ^{1}H (900 MHz) and ^{13}C (225 MHz) NMR spectra were recorded on a Bruker Avance Neo 21.1 T spectrometer equipped with a 3.2 mm low-temperature CPMAS probe. ^{133}Cs shifts were referenced to 1 M aqueous solution of CsCl, using solid CsI (δ=271.05 ppm) as a secondary reference. ^{1}H and ^{13}C chemical shifts were referenced to solid adamantane (δ_H=1.91 ppm and δ_C=29.45 (CH) and 38.48 (CH_2) ppm). Low-temperature ^{1}H-^{31}P cross-polarization (CP) experiments used 1 ms optimized contact pulses, 63 kHz SPINAL-64 ^{1}H decoupling and the following recycle delays: 1.7 s (δ-$FAPbI_3$), 3 s (α-$FAPbI_3$), 22 s ($FA_{0.16}Cs_{0.84}PbI_3$), Quantitative echo-detected ^{133}Cs spectra used a recycle delay of 400 s. ^{1}H spectra were acquired with recycle delays between 2 and 20 s. Peak widths were fitted in Topspin 3.2 and the uncertainties are given at one standard deviation.

Conflicts of interest

"There are no conflicts to declare".

Acknowledgement

U.R. gratefully acknowledges funding from the Swiss National Science Foundation via individual grant No. 200020-185092, the NCCR MUST and the Sinergia grant EPISODE. D.J.K, A.M. and L.E. are grateful for financial support from Swiss National Science Foundation Grant No. 200020_178860. The authors thank the Swiss National Supercomputing Centre (CSCS) for the computer time.

Supporting Information Available

References

(1) Kojima, A.; Teshima, K.; Shirai, Y.; Miyasaka, T. Organometal Halide Perovskites as Visible-Light Sensitizers for Photovoltaic Cells. *J. Am. Chem. Soc.* **2009**, *131*, 6050–6051.

(2) Im, J.-H.; Lee, C.-R.; Lee, J.-W.; Park, S.-W.; Park, N.-G. 6.5% Efficient Perovskite Quantum-Dot-Sensitized Solar Cell. *Nanoscale* **2011**, *3*, 4088–4093.

(3) Kim, H.-S.; Lee, C.-R.; Im, J.-H.; Lee, K.-B.; Moehl, T.; Marchioro, A.; Moon, S.-J.; Humphry-Baker, R.; Yum, J.-H.; Moser, J. E.; Grätzel, M.; Park, N.-G. Lead Iodide Perovskite Sensitized All-Solid-State Submicron Thin Film Mesoscopic Solar Cell with Efficiency Exceeding 9%. *Sci. Rep. 2*, 591.

(4) Lee, M. M.; Teuscher, J.; Miyasaka, T.; Murakami, T. N.; Snaith, H. J. Efficient Hybrid

Solar Cells Based on Meso-Superstructured Organometal Halide Perovskites. *Science* **2012**, *338*, 643–647.

(5) Etgar, L.; Gao, P.; Xue, Z.; Peng, Q.; Chandiran, A. K.; Liu, B.; Nazeeruddin, M. K.; Grätzel, M. Mesoscopic $CH_3NH_3PbI_3/TiO_2$ Heterojunction Solar Cells. *J. Am. Chem. Soc.* **2012**, *134*, 17396–17399.

(6) Mei, A.; Li, X.; Liu, L.; Ku, Z.; Liu, T.; Rong, Y.; Xu, M.; Hu, M.; Chen, J.; Yang, Y.; Grätzel, M.; Han, H. A Hole-Conductor–Free, Fully Printable Mesoscopic Perovskite Solar Cell with High Stability. *Science* **2014**, *345*, 295–298.

(7) Eperon, G. E.; Stranks, S. D.; Menelaou, C.; Johnston, M. B.; Herz, L. M.; Snaith, H. J. Formamidinium Lead Trihalide: a Broadly Tunable Perovskite for Efficient Planar Heterojunction Solar Cells. *Energy Environ. Sci.* **2014**, *7*, 982–988.

(8) Kim, H.-S.; Lee, C.-R.; Im, J.-H.; Lee, K.-B.; Moehl, T.; Marchioro, A.; Moon, S.-J.; Humphry-Baker, R.; Yum, J.-H.; Moser, J. E., et al. Lead Iodide Perovskite Sensitized All-Solid-State Submicron Thin Film Mesoscopic Solar Cell with Efficiency Exceeding 9 %. *Sci. Rep.* **2012**, *2*, 591.

(9) Shockley, W.; Queisser, H. J. Detailed Balance Limit of Efficiency of p-n Junction Solar Cells. *J. Appl. Phys.* **1961**, *32*, 510–519.

(10) Rühle, S. Tabulated Values of the Shockley–Queisser Limit for Single Junction Solar Cells. *Sol. Energy* **2016**, *130*, 139–147.

(11) Huang, Z.; Wang, D.; Wang, S.; Zhang, T. Highly Efficient and Stable $MAPbI_3$ Perovskite Solar Cell Induced by Regulated Nucleation and Ostwald Recrystallization. *Materials* **2018**, *11*, 778.

(12) Pang, S.; Hu, H.; Zhang, J.; Lv, S.; Yu, Y.; Wei, F.; Qin, T.; Xu, H.; Liu, Z.; Cui, G.

$NH_2CH{=}NH_2PbI_3$: An Alternative Organolead Iodide Perovskite Sensitizer for Mesoscopic Solar Cells. *Chem. Mater.* **2014**, *26*, 1485–1491.

(13) Koh, T. M.; Fu, K.; Fang, Y.; Chen, S.; Sum, T. C.; Mathews, N.; Mhaisalkar, S. G.; Boix, P. P.; Baikie, T. Formamidinium-Containing Metal-Halide: An Alternative Material for Near-IR Absorption Perovskite Solar Cells. *J. Phys. Chem. C* **2014**, *118*, 16458–16462.

(14) Jeon, N. J.; Noh, J. H.; Yang, W. S.; Kim, Y. C.; Ryu, S.; Seo, J.; Seok, S. I. Compositional Engineering of Perovskite Materials for High-Performance Solar Cells. *Nature* **2015**, *517*, 476.

(15) Stoumpos, C. C.; Malliakas, C. D.; Peters, J. A.; Liu, Z.; Sebastian, M.; Im, J.; Chasapis, T. C.; Wibowo, A. C.; Chung, D. Y.; Freeman, A. J.; Wessels, B. W.; Kanatzidis, M. G. Crystal Growth of the Perovskite Semiconductor $CsPbBr_3$: A New Material for High-Energy Radiation Detection. *Cryst. Growth Des.* **2013**, *13*, 2722–2727.

(16) Trots, D. M.; Myagkota, S. V. High-Temperature Structural Evolution of Caesium and Rubidium Triiodoplumbates. *J. Phys. Chem. Solids* **2008**, *69*, 2520–2526.

(17) Møller, C. K. Crystal Structure and Photoconductivity of Caesium Plumbohalides. *Nature 182*, 1436.

(18) Eperon, G. E.; Paternò, G. M.; Sutton, R. J.; Zampetti, A.; Haghighirad, A. A.; Cacialli, F.; Snaith, H. J. Inorganic Caesium Lead Iodide Perovskite Solar Cells. *J. Mater. Chem. A* **2015**, *3*, 19688–19695.

(19) Coutts, T. J.; Emery, K. A.; Scott Ward, J. Modeled Performance of Polycrystalline Thin-Film Tandem Solar Cells. *Prog Photovolt 10*, 195–203.

(20) Bailie, C. D.; Christoforo, M. G.; Mailoa, J. P.; Bowring, A. R.; Unger, E. L.; Nguyen, W. H.; Burschka, J.; Pellet, N.; Lee, J. Z.; Grätzel, M.; Noufi, R.; Buonassisi, T.; Salleo, A.; McGehee, M. D. Semi-Transparent Perovskite Solar Cells for Tandems with Silicon and CIGS. *Energy Environ. Sci.* **2015**, *8*, 956–963.

(21) Todorov, T.; Gershon, T.; Gunawan, O.; Sturdevant, C.; Guha, S. Perovskite-Kesterite Monolithic Tandem Solar Cells with High Open-Circuit Voltage. *Appl. Phys. Lett.* **2014**, *105*, 173902.

(22) Bailie, C. D.; McGehee, M. D. High-Efficiency Tandem Perovskite Solar Cells. *MRS Bull.* **2015**, *40*, 681–686.

(23) Leijtens, T.; Bush, K. A.; Prasanna, R.; McGehee, M. D. Opportunities and Challenges for Tandem Solar Cells using Metal Halide Perovskite Semiconductors. *Nat. Energy* **2018**, 2058–7546.

(24) Stoumpos, C. C.; Malliakas, C. D.; Kanatzidis, M. G. Semiconducting Tin and Lead Iodide Perovskites with Organic Cations: Phase Transitions, High Mobilities, and Near-Infrared Photoluminescent Properties. *Inorg. Chem.* **2013**, *52*, 9019–9038.

(25) Wang, Y.; Dar, M. I.; Ono, L. K.; Zhang, T.; Kan, M.; Li, Y.; Zhang, L.; Wang, X.; Yang, Y.; Gao, X., et al. Thermodynamically Stabilized β-$CsPbI_3$-Based Perovskite Solar Cells with Efficiencies >18%. *Science* **2019**, *365*, 591–595.

(26) Stoumpos, C. C.; Kanatzidis, M. G. The Renaissance of Halide Perovskites and Their Evolution as Emerging Semiconductors. *Acc. Chem. Res.* **2015**, *48*, 2791–2802.

(27) Lai, M.; Kong, Q.; Bischak, C. G.; Yu, Y.; Dou, L.; Eaton, S. W.; Ginsberg, N. S.; Yang, P. Structural, Optical, and Electrical Properties of Phase-Controlled Cesium Lead Iodide Nanowires. *Nano Res.* **2017**, *10*, 1107–1114.

(28) Sutton, R. J.; Filip, M. R.; Haghighirad, A. A.; Sakai, N.; Wenger, B.; Giustino, F.; Snaith, H. J. Cubic or Orthorhombic? Revealing the Crystal Structure of Metastable Black-phase $CsPbI_3$ by Theory and Experiment. *ACS Energy Lett.* **2018**,

(29) Ke, W.; Spanopoulos, I.; Stoumpos, C. C.; Kanatzidis, M. G. Myths and Reality of $HPbI_3$ in Halide Perovskite Solar Cells. *Nat. Commun.* **2018**, *9*, 4785.

(30) Wang, Y.; Dar, M. I.; Ono, L. K.; Zhang, T.; Kan, M.; Li, Y.; Zhang, L.; Wang, X.; Yang, Y.; Gao, X.; Qi, Y.; Grätzel, M.; Zhao, Y. Thermodynamically Stabilized β-$CsPbI_3$–Based Perovskite Solar Cells with Efficiencies >18%. *Science* **2019**, *365*, 591–595.

(31) Pellet, N.; Gao, P.; Gregori, G.; Yang, T.-Y.; Nazeeruddin, M. K.; Maier, J.; Grätzel, M. Mixed-Organic-Cation Perovskite Photovoltaics for Enhanced Solar-Light Harvesting. *Angew. Chem. 53*, 3151–3157.

(32) Saliba, M.; Matsui, T.; Seo, J.-Y.; Domanski, K.; Correa-Baena, J.-P.; Nazeeruddin, M. K.; Zakeeruddin, S. M.; Tress, W.; Abate, A.; Hagfeldt, A.; Grätzel, M. Cesium-Containing Triple Cation Perovskite Solar Cells: Improved Stability, Reproducibility and High Efficiency. *Energy Environ. Sci.* **2016**, *9*, 1989–1997.

(33) Saliba, M.; Matsui, T.; Domanski, K.; Seo, J.-Y.; Ummadisingu, A.; Zakeeruddin, S. M.; Correa-Baena, J.-P.; Tress, W. R.; Abate, A.; Hagfeldt, A.; Grätzel, M. Incorporation of Rubidium Cations into Perovskite Solar Cells Improves Photovoltaic Performance. *Science* **2016**, *354*, 206–209.

(34) Choi, H.; Jeong, J.; Kim, H.-B.; Kim, S.; Walker, B.; Kim, G.-H.; Kim, J. Y. Cesium-Doped Methylammonium Lead Iodide Perovskite Light Absorber for Hybrid Solar Cells. *Nano Energy* **2014**, *7*, 80–85.

(35) Lee, J.-W.; Kim, D.-H.; Kim, H.-S.; Seo, S.-W.; Cho, S. M.; Park, N.-G. Formamidinium

and Cesium Hybridization for Photo- and Moisture-Stable Perovskite Solar Cell. *Adv. Energy Mater. 5*, 1501310.

(36) Yi, C.; Luo, J.; Meloni, S.; Boziki, A.; Ashari-Astani, N.; Grätzel, C.; Zakeeruddin, S. M.; Röthlisberger, U.; Grätzel, M. Entropic Stabilization of Mixed A-Cation ABX_3 Metal Halide Perovskites for High Performance Perovskite Solar Cells. *Energy Environ. Sci.* **2016**, *9*, 656–662.

(37) Li, Z.; Yang, M.; Park, J.-S.; Wei, S.-H.; Berry, J. J.; Zhu, K. Stabilizing Perovskite Structures by Tuning Tolerance Factor: Formation of Formamidinium and Cesium Lead Iodide Solid-State Alloys. *Chem. Mater.* **2016**, *28*, 284–292.

(38) Goldschmidt, V. M. Die Gesetze der Krystallochemie. *Naturwissenschaften* **1926**, *14*, 477–485.

(39) Mitzi, D. B. Templating and Structural Engineering in Organic–Inorganic Perovskites. *J. Chem. Soc., Dalton Trans.* **2001**, 1–12.

(40) Kieslich, G.; Sun, S.; Cheetham, A. K. Solid-State Principles Applied to Organic–Inorganic Perovskites: New Tricks for an Old Dog. *Chem. Sci.* **2014**, *5*, 4712–4715.

(41) Kieslich, G.; Sun, S.; Cheetham, A. K. An Extended Tolerance Factor Approach for Organic-Inorganic Perovskites. *Chem. Sci.* **2015**, *6*, 3430–3433.

(42) Perdew, J. P.; Burke, K.; Wang, Y. Generalized Gradient Approximation for the Exchange-Correlation Hole of a Many-Electron System. *Phys. Rev. B* **1996**, *54*, 16533–16539.

(43) Wiktor, J.; Rothlisberger, U.; Pasquarello, A. Predictive Determination of Band Gaps of Inorganic Halide Perovskites. *J. Phys. Chem. Lett.* **2017**, *8*, 5507–5512.

(44) Meloni, S.; Palermo, G.; Ashari-Astani, N.; Grätzel, M.; Rothlisberger, U. Valence and Conduction Band Tuning in Halide Perovskites for Solar Cell Applications. *J. Mater. Chem. A* **2016**, *4*, 15997–16002.

(45) Dar, M. I.; Jacopin, G.; Meloni, S.; Mattoni, A.; Arora, N.; Boziki, A.; Zakeeruddin, S. M.; Rothlisberger, U.; Grätzel, M. Origin of Unusual Bandgap Shift and Dual Emission in Organic-Inorganic Lead Halide Perovskites. *Sci. Adv.* **2016**, *2*.

(46) Vydrov, O. A.; Van Voorhis, T. Nonlocal Van der Waals Density Functional: The simpler the Better. *J. Chem. Phys.* **2010**, *133*, 244103.

(47) Sabatini, R.; Gorni, T.; de Gironcoli, S. Nonlocal Van der Waals Density Functional Made Simple and Efficient. *Phys. Rev. B* **2013**, *87*, 041108.

(48) Brivio, F.; Frost, J. M.; Skelton, J. M.; Jackson, A. J.; Weber, O. J.; Weller, M. T.; Goñi, A. R.; Leguy, A. M. A.; Barnes, P. R. F.; Walsh, A. Lattice Dynamics and Vibrational Spectra of the Orthorhombic, Tetragonal, and Cubic Phases of Methylammonium Lead Iodide. *Phys. Rev. B* **2015**, *92*, 144308.

(49) Meloni, S.; Moehl, T.; Tress, W.; Franckevičius, M.; Saliba, M.; Lee, Y. H.; Gao, P.; Nazeeruddin, M. K.; Zakeeruddin, S. M.; Rothlisberger, U., et al. Ionic Polarization-Induced Current-Voltage Hysteresis in $CH_3NH_3PbX_3$ Perovskite Solar Cells. *Nat. Commun.* **2016**, *7*, 10334.

(50) Prochowicz, D.; Franckevičius, M.; Cieślak, A.; Zakeeruddin, S.; Grätzel, M.; Lewiński, J. Mechanosynthesis of the Hybrid Perovskite $CH_3NH_3PbI_3$: Characterization and the Corresponding Solar Cell Efficiency. *J. Mater. Chem. A* **2015**, *3*, 20772–20777.

(51) Prochowicz, D.; Yadav, P.; Saliba, M.; Saski, M.; Zakeeruddin, S.; Lewiński, J.; Grätzel, M. Mechanosynthesis of Pure Phase Mixed-Cation $MA_xFA_{1-x}PbI_3$ Hybrid

Perovskites: Photovoltaic Performance and Electrochemical Properties. *Sustain. Energy Fuels* **2017**, *1*, 689–693.

(52) Rosales, B. A.; Wei, L.; Vela, J. Synthesis and Mixing of Complex Halide Perovskites by Solvent-Free Solid-State Methods. *J. Solid State Chem.* **2019**, *271*, 206–215.

(53) Kubicki, D. J.; Prochowicz, D.; Hofstetter, A.; Pechy, P.; Zakeeruddin, S. M.; Grätzel, M.; Emsley, L. Cation Dynamics in Mixed-Cation $(MA)_x(FA)_{1-x}PbI_3$ Hybrid Perovskites from Solid-State NMR. *J. Am. Chem. Soc.* **2017**, *139*, 10055–10061.

(54) Kubicki, D. J.; Prochowicz, D.; Hofstetter, A.; Saski, M.; Yadav, P.; Bi, D.; Pellet, N.; Lewiński, J.; Zakeeruddin, S. M.; Grätzel, M., et al. Formation of Stable Mixed Guanidinium-Methylammonium Phases with Exceptionally Long Carrier Lifetimes for High-Efficiency Lead Iodide-Based Perovskite Photovoltaics. *J. Am. Chem. Soc.* **2018**, *140*, 3345–3351.

(55) Kubicki, D. J.; Prochowicz, D.; Hofstetter, A.; Zakeeruddin, S. M.; Grätzel, M.; Emsley, L. Phase Segregation in Potassium-Doped Lead Halide Perovskites from 39 K solid-state NMR at 21.1 T. *J. Am. Chem. Soc.* **2018**, *140*, 7232–7238.

(56) Bi, D.; Li, X.; Milić, J. V.; Kubicki, D. J.; Pellet, N.; Luo, J.; LaGrange, T.; Mettraux, P.; Emsley, L.; Zakeeruddin, S. M., et al. Multifunctional Molecular Modulators for Perovskite Solar Cells with over 20% Efficiency and High Operational Stability. *Nat. Commun.* **2018**, *9*, 4482.

(57) Tavakoli, M. M.; Tress, W.; Milić, J. V.; Kubicki, D.; Emsley, L.; Grätzel, M. Addition of Adamantylammonium Iodide to Hole Transport Layers Enables Highly Efficient and Electroluminescent Perovskite Solar Cells. *Energy Environ. Sci.* **2018**, *11*, 3310–3320.

(58) Kubicki, D. J.; Prochowicz, D.; Pinon, A.; Stevanato, G.; Hofstetter, A.; Zakeeruddin, S. M.; Grätzel, M.; Emsley, L. Doping and Phase Segregation in Mn^{2+}-and Co^{2+}-

Doped Lead Halide Perovskites from ^{133}Cs and ^{1}H NMR Relaxation Enhancement. *J. Mater. Chem. A* **2019**, *7*, 2326–2333.

(59) Rosales, B. A.; Men, L.; Cady, S. D.; Hanrahan, M. P.; Rossini, A. J.; Vela, J. Persistent Dopants and Phase Segregation in Organolead Mixed-Halide Perovskites. *Chem. Mater.* **2016**, *28*, 6848–6859.

(60) Rosales, B. A.; Hanrahan, M. P.; Boote, B. W.; Rossini, A. J.; Smith, E. A.; Vela, J. Lead Halide Perovskites: Challenges and Opportunities in Advanced Synthesis and Spectroscopy. *ACS Energy Lett.* **2017**, *2*, 906–914.

(61) Karmakar, A.; Askar, A. M.; Bernard, G. M.; Terskikh, V. V.; Ha, M.; Patel, S.; Shankar, K.; Michaelis, V. K. Mechanochemical Synthesis of Methylammonium Lead Mixed-Halide Perovskites: Unraveling the Solid-Solution Behavior Using Solid-State NMR. *Chem. Mater.* **2018**, *30*, 2309–2321.

(62) Kubicki, D. J.; Prochowicz, D.; Hofstetter, A.; Zakeeruddin, S. M.; Grätzel, M.; Emsley, L. Phase Segregation in Cs-, Rb-and K-Doped Mixed-Cation $(MA)_x(FA)_{1-x}PbI_3$ Hybrid Perovskites from Solid-State NMR. *J. Am. Chem. Soc.* **2017**, *139*, 14173–14180.

(63) Xiang, W.; Wang, Z.; Kubicki, D. J.; Tress, W.; Luo, J.; Prochowicz, D.; Akin, S.; Emsley, L.; Zhou, J.; Dietler, G., et al. Europium-Doped $CsPbI_2Br$ for Stable and Highly Efficient Inorganic Perovskite Solar Cells. *Joule* **2019**, *3*, 205–214.

(64) Prochowicz, D.; Yadav, P.; Saliba, M.; Kubicki, D. J.; Tavakoli, M. M.; Zakeeruddin, S. M.; Lewiński, J.; Emsley, L.; Grätzel, M. One-step Mechanochemical Incorporation of an Insoluble Cesium Additive for High Performance Planar Heterojunction Solar Cells. *Nano Energy* **2018**, *49*, 523–528.

(65) Karmakar, A.; Dodd, M. S.; Agnihotri, S.; Ravera, E.; Michaelis, V. K. Cu(II)-Doped $Cs_2SbAgCl_6$ Double Perovskite: A Lead-Free, Low-Bandgap Material. *Chem. Mater.* **2018**, *30*, 8280–8290.

(66) Karmakar, A.; Dodd, M. S.; Zhang, X.; Oakley, M. S.; Klobukowski, M.; Michaelis, V. K. Mechanochemical Synthesis of 0D and 3D Cesium Lead Mixed Halide Perovskites. *Chem. Commun.* **2019**, *55*, 5079–5082.

(67) Even, J.; Pedesseau, L.; Jancu, J.-M.; Katan, C. Importance of Spin–Orbit Coupling in Hybrid Organic/Inorganic Perovskites for Photovoltaic Applications. *J. Phys. Chem. Lett.* **2013**, *4*, 2999–3005.

(68) Umari, P.; Mosconi, E.; De Angelis, F. Relativistic GW calculations on $CH_3NH_3PbI_3$ and $CH_3NH_3SnI_3$ Perovskites for Solar Cell Applications. *Sci. Rep. 4*, 4467.

(69) Ashari-Astani, N.; Meloni, S.; Salavati, A. H.; Palermo, G.; Grätzel, M.; Rothlisberger, U. Computational Characterization of the Dependence of Halide Perovskite Effective Masses on Chemical Composition and Structure. *J. Phys. Chem. C* **2017**, *121*, 23886–23895.

(70) Hohenberg, P.; Kohn, W. Inhomogeneous Electron Gas. *Phys. Rev.* **1964**, *136*, B864–B871.

(71) Kohn, W.; Sham, L. J. Self-Consistent Equations Including Exchange and Correlation Effects. *Phys. Rev.* **1965**, *140*, A1133–A1138.

(72) Giannozzi, P. et al. QUANTUM ESPRESSO: a Modular and Open-Source Software Project for Quantum Simulations of Materials. *J. Phys. Condens. Matter* **2009**, *21*, 395502.

(73) Giannozzi, P. et al. Advanced Capabilities for Materials Modelling with Quantum ESPRESSO. *J. Phys. Condens. Matter* **2017**, *29*, 465901.

(74) Corso, A. D. Pseudopotentials Periodic Table: From H to Pu. *Comput. Mater. Sci.* **2014**, *95*, 337–350.

(75) Monkhorst, H. J.; Pack, J. D. Special Points for Brillouin-Zone Integrations. *Phys. Rev. B* **1976**, *13*, 5188–5192.

(76) Alkauskas, A.; Broqvist, P.; Pasquarello, A. Defect Energy Levels in Density Functional Calculations: Alignment and Band Gap Problem. *Phys. Rev. Lett.* **2008**, *101*, 046405.

(77) CPMD, http://www.cpmd.org/, Copyright IBM Corp 1990-2015, Copyright MPI für Festkörperforschung Stuttgart 1997-2001.

(78) Goedecker, S.; Teter, M.; Hutter, J. Separable Dual-Space Gaussian Pseudopotentials. *Phys. Rev. B* **1996**, *54*, 1703–1710.

(79) Hartwigsen, C.; Goedecker, S.; Hutter, J. Relativistic Separable Dual-Space Gaussian Pseudopotentials from H to Rn. *Phys. Rev. B* **1998**, *58*, 3641–3662.

(80) Krack, M. Pseudopotentials for H to Kr Optimized for Gradient-Corrected Exchange-Correlation Functionals. *Theor. Chem. Acc.* **2005**, *114*, 145–152.

(81) Nosé, S. A Molecular Dynamics Method for Simulations in the Canonical Ensemble. *Mol. Phys.* **1984**, *52*, 255–268.

(82) Nosé, S. A Unified Formulation of the Constant Temperature Molecular Dynamics Methods. *J. Chem. Phys.* **1984**, *81*, 511–519.

(83) Hoover, W. G. Canonical Dynamics: Equilibrium Phase-Space Distributions. *Phys. Rev. A* **1985**, *31*, 1695–1697.

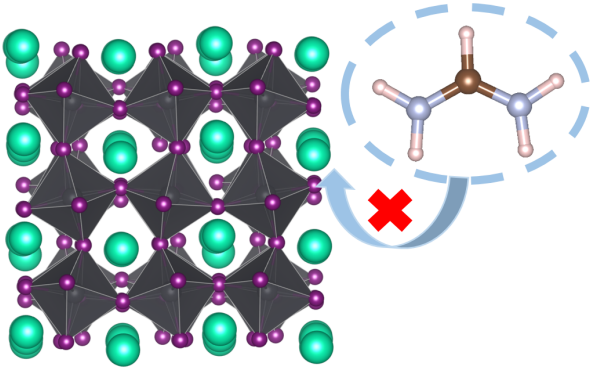

Figure 10: For Table of Contents Only

Atomistic origins of the limited phase stability of Cs^+-rich $FA_xCs_{(1-x)}PbI_3$ mixtures - Supporting Information

Ariadni Boziki,[†] Dominik J. Kubicki,[‡,§] Aditya Mishra,[‡] Simone Meloni,[†,‖] Lyndon Emsley,[‡] Michael Grätzel,[¶] and Ursula Rothlisberger[*,†]

†*Laboratory of Computational Chemistry and Biochemistry, Institute of Chemical Sciences and Engineering, École Polytechnique Fédérale de Lausanne, CH-1015 Lausanne, Switzerland.*

‡*Laboratory of Magnetic Resonance, Institute of Chemical Sciences and Engineering, École Polytechnique Fédérale de Lausanne, CH-1015 Lausanne, Switzerland.*

¶*Laboratory of Photonics and Interfaces, Institute of Chemical Sciences and Engineering, École Polytechnique Fédérale de Lausanne, CH-1015 Lausanne, Switzerland.*

§*Current address: Cavendish Laboratory, JJ Thomson Avenue, Cambridge CB3 0HE, United Kingdom.*

‖*Current address: Dipartimento di Scienze Chimiche e Farmaceutiche (DipSCF), Universita' degli Studi di Ferrara - Unife, Via Luigi Borsari 46, I-44121, Ferrara, Italy.*

E-mail: ursula.roethlisberger@epfl.ch

Phone: +41 (0)21 693 03 21. Fax: +41 (0)21 693 03 20

Finite temperature effects

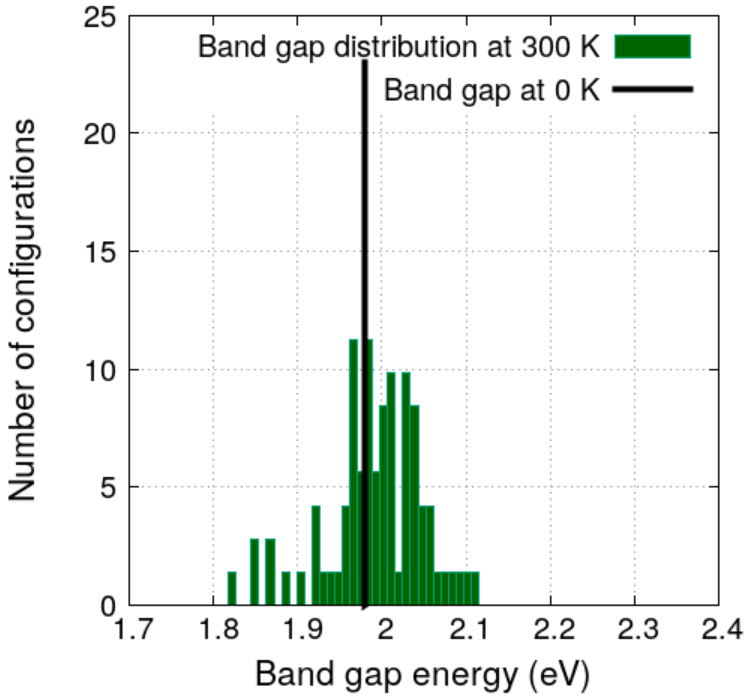

Figure S1: Histogram of the thermal distribution of the Kohn-Sham band gaps for the orthorhombic phase of $CsPbI_3$.

Table S1: Goldschmidt tolerance factors calculated for both pure compounds and mixtures.

Fraction of FA^+ doped into $CsPbI_3$ structure	Goldschmidt tolerance factor
0%	0.81
8%	0.82
17%	0.84
25%	0.85
33%	0.87
42%	0.88
50%	0.90
100%	0.99

Relative stability

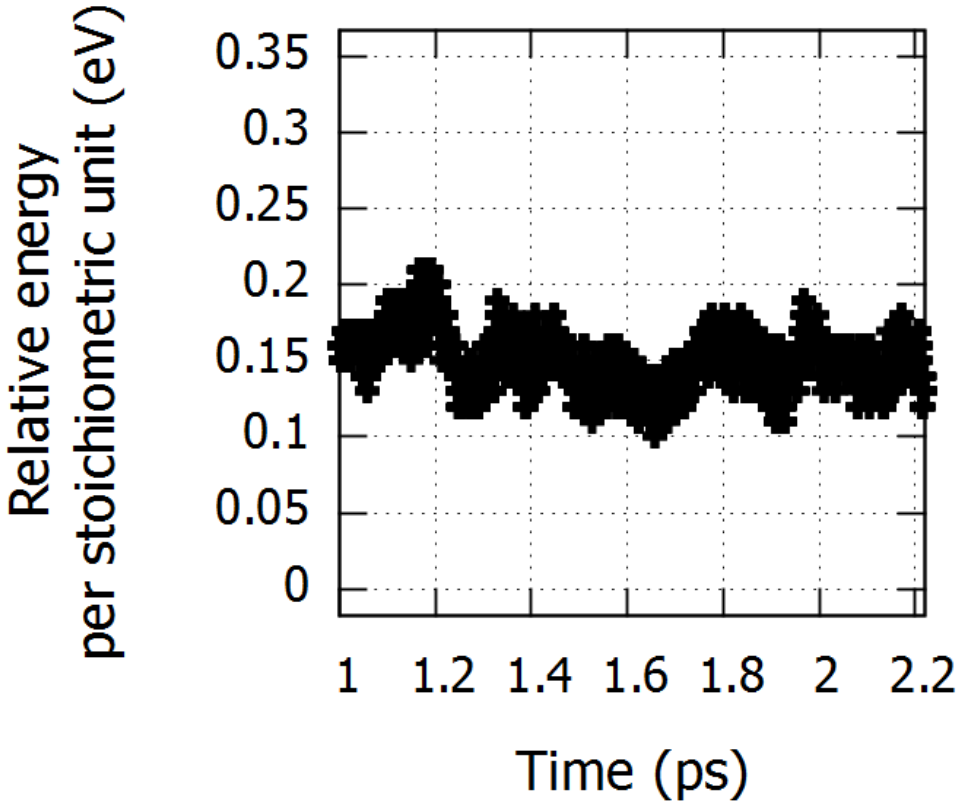

Figure S2: Relative energy difference per stoichiometric unit for each frame between δ and perovskite $FA_{0.33}Cs_{0.67}PbI_3$ mixtures across a 2.2 ps trajectory from MD simulations. The δ phase is always more stable than the perovskite phase.

XRD characterization

XRD patterns were recorded on an X'Pert MPD PRO (Panalytical) diffractometer equipped with a ceramic tube (Cu anode, $\lambda = 1.54060$), a secondary graphite (002) monochromator and an RTMS X'Celerator detector (Panalytical) in an angle range of $2\theta = 5°$ to $40°$, by step scanning with a step of 0.02 degree.

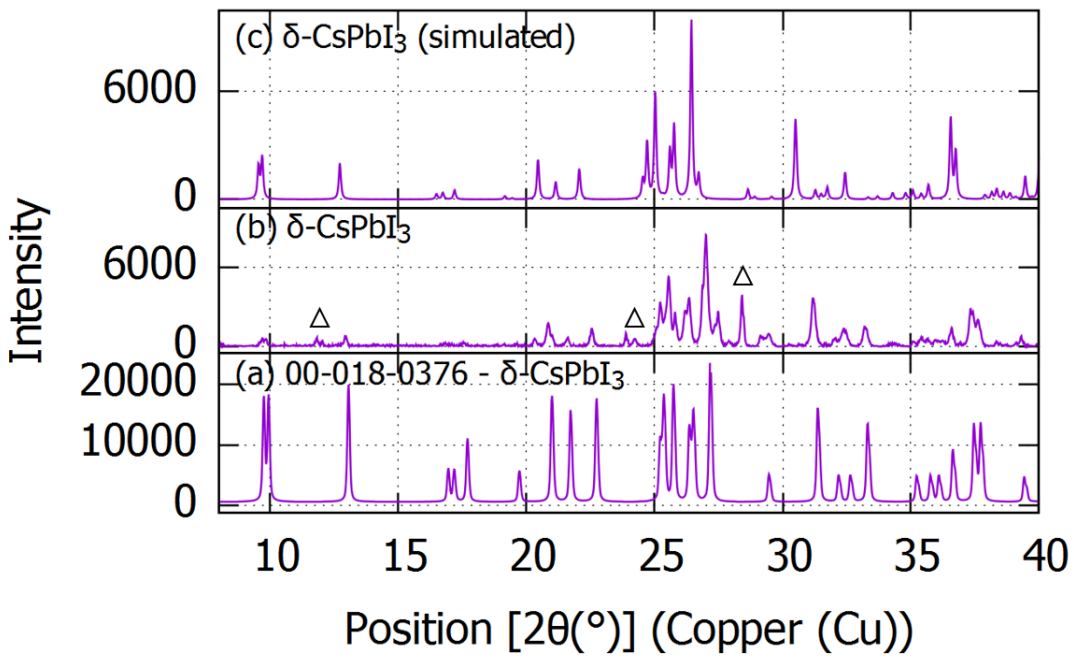

Figure S3: Powder XRD characterization of the pure materials. (a) reference δ-$CsPbI_3$ pattern (ICDD number: 00-018-0376). Experimental pattern: (b) δ-$CsPbI_3$. '△' indicate an impurity phase (Cs_4PbI_6). Simulated powder XRD pattern with $\lambda = 1.54056$ and h,k,l=0,7,-5, in an angle range of $2\theta = 5°$ to $50°$, by step scanning with a step of 0.02 degree: (c) δ-$CsPbI_3$.

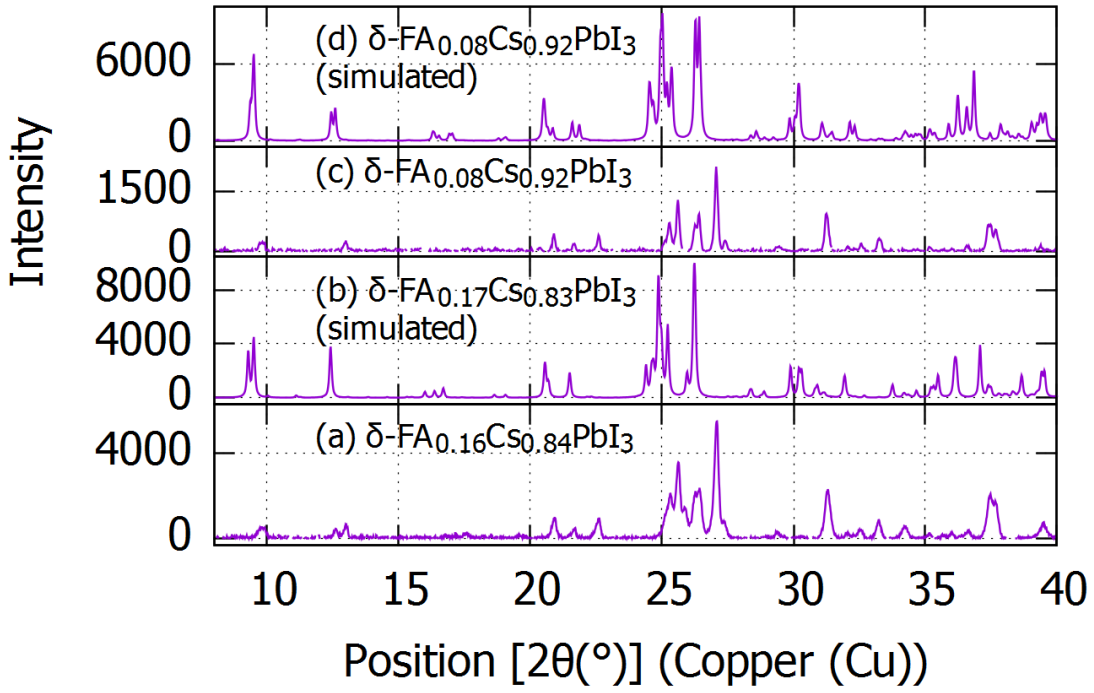

Figure S4: Powder XRD characterization of the mixtures. Experimental patterns: (a) δ-$FA_{0.16}Cs_{0.84}PbI_3$, (c) δ-$FA_{0.08}Cs_{0.92}PbI_3$. Simulated powder XRD patterns with $\lambda = 1.54056$ and h,k,l=0,7,-5, in an angle range of $2\theta = 5°$ to $50°$, by step scanning with a step of 0.02 degree. (b) δ-$FA_{0.17}Cs_{0.83}PbI_3$, (d) δ-$FA_{0.08}Cs_{0.92}PbI_3$.